Title

Organic matter in carbonaceous chondrite lithologies of Almahata Sitta: Incorporation of previously unsampled carbonaceous chondrite lithologies into ureilitic regolith

Journal

Meteoritics and Planetary Science, 56(7)

ISSN

1086-9379

Authors

Kebukawa, Yoko
Zolensky, Michael E
Goodrich, Cyrena A
et al.

Publication Date

2021-07-01

DOI

10.1111/maps.13713

Peer reviewed

Organic matter in carbonaceous chondrite lithologies of Almahata Sitta: Incorporation of previously unsampled carbonaceous chondrite lithologies into ureilitic regolith

Yoko Kebukawa[1]*, Michael. E. Zolensky[2], Cyrena A. Goodrich[3], Motoo Ito[4], Nanako O. Ogawa[5], Yoshinori Takano[5], Naohiko Ohkouchi[5], Kento Kiryu[1], Motoko Igisu[6], Takazo Shibuya[6], Matthew A. Marcus[7], Takuji Ohigashi[8], James Martinez[9], Yu Kodama[10], Muawia H. Shaddad[11], and Peter Jenniskens[12]

*Corresponding author email: kebukawa@ynu.ac.jp

[1] Department of Chemistry and Life Science, Yokohama National University, 79-5 Tokiwadai, Hodogaya-ku, Yokohama 240-8501, Japan

[2] Astromaterials Research and Exploration Science, NASA Johnson Space Center, 2101 NASA Parkway, Houston, TX 77058, USA

[3] Lunar and Planetary Institute, Universities Space Research Association-Houston, 3600 Bay Area Blvd, Houston, TX 77058 USA,

[4] Kochi Institute for Core Sample Research, Japan Agency for Marine-Earth Science and Technology (JAMSTEC), B200 Monobe, Nankoku, Kochi 783-8502, Japan

[5] Biogeochemistry Research Center (BGC), Japan Agency for Marine-Earth Science and Technology (JAMSTEC), 2-15 Natsushima-Cho, Yokosuka 237-0061, Japan

[6] Super-cutting-edge Grand and Advanced Research (Sugar) Program, Institute for Extra-cutting-edge Science and Technology Avant-garde Research (X-star), Japan Agency for Marine-Earth Science and Technology (JAMSTEC), 2-15 Natsushima-cho, Yokosuka 237-0061, Japan

[7] Advanced Light Source, Lawrence Berkeley National Laboratory, 1 Cyclotron Road, Berkeley, CA 94720, USA

[8] UVSOR Synchrotron, Institute for Molecular Science, 38 Nishigo-Naka, Myodaiji, Okazaki 444-

8585, Japan
[9] Jacobs Engineering, NASA Johnson Space Center, 2101 NASA Parkway, Houston, TX 77058, USA
[10] Marine Works Japan Ltd., B200 Monobe, Nankoku, Kochi 783-8502, Japan
[11] Physics Department, University of Khartoum, Khartoum 11115, Sudan
[12] SETI Institute, 189 Bernardo Ave, Mountain View, CA 94043, USA

Abstract

The Almahata Sitta (AhS) meteorite is a unique polymict ureilite. Recently, carbonaceous chondritic lithologies were identified in AhS. Organic matter (OM) is ubiquitously found in primitive carbonaceous chondrites. The molecular and isotopic characteristics of this OM reflect its origin and parent body processes, and are particularly sensitive to heating. The C1-lithologies, AhS 671 and AhS 91A were investigated, focusing mainly on the OM. We found that the OM in these lithologies is unique and contains primitive isotopic signatures, but experienced slight heating possibly by short-term heating event(s). These characteristics support the idea that one or more carbonaceous chondritic bodies were incorporated into the ureilitic parent body. The uniqueness of the OM in the AhS samples implies that there were large variations in primitive carbonaceous chondritic materials in the Solar System other than known primitive carbonaceous chondrite groups such as CI, CM, and CR chondrites.

INTRODUCTION

Organic matter (OM) is ubiquitously found in primitive carbonaceous chondrites (CCs). The majority of OM is found in the form of complex macromolecular organic materials that are often referred to as insoluble organic matter (IOM). The fraction of soluble organic matter (SOM) is relatively small, but its compositional variation is huge—thousands of different molecular formulae exist including further alteration products of organic molecules (e.g., Orthous-Daunay et al. 2019; Schmitt-Kopplin et al. 2010). The total amount of OM in thermally metamorphosed carbonaceous, ordinary, and enstatite

chondrites is drastically lower compared to unheated (CI, CM, and CR) CCs, due to high temperature processing which decomposes the OM (e.g., Alexander et al. 2007). The elemental and isotopic compositions and molecular structures of OM reflect their parent body processes and are particularly sensitive to heating (e.g., Alexander et al. 2007; Alexander et al. 2010; Kebukawa et al. 2011; Quirico et al. 2018). Thus, OM in chondrites can be used as indicators of thermal events (Busemann et al. 2007; Cody et al. 2008; Kebukawa et al. 2010). In contrast, with the exception of ureilites, differentiated meteorites rarely contain carbonaceous compounds other than xenolithic material.

The ureilites are a group of primitive achondrites. Main group ureilites mainly consist of olivine and pyroxene, and are characterized by high abundances of carbon, principally in the form of well-crystalline graphite as well as minor diamond. They represent the residual mantle of a carbon-rich parent asteroid that experienced high-temperature igneous processing and partial differentiation early in the history of the solar system (Collinet and Grove 2020; Goodrich et al. 2015; Goodrich et al. 2007; Mittlefehldt et al. 1998; Scott et al. 1993; Warren and Kallemeyn 1992). Polymict ureilites are breccias consisting of mixed ureilitic materials, as well as an important component of xenolith clasts, including multiple chondritic and non-ureilitic achondrite types. Polymict ureilites represent regolith formed on ureilitic offspring bodies that accreted as rubble piles after catastrophic disruption of a primordial ureilite parent body (e.g., Goodrich et al. 2015). The Almahata Sitta (AhS) meteorite is considered to be an anomalous polymict ureilite. AhS originated from the impact of the near-earth asteroid 2008 TC_3, which is tentatively classified as an F-type asteroid (a subtype in C complex) in spectroscopic taxonomy (Jenniskens et al. 2009). The asteroid disintegrated in the atmosphere and the recovered stones, which include a wide variety of different meteorite types, represent clasts from the pre-impact breccia. Approximately 50-70% of the AhS stones are ureilitic materials and the rest include a wide variety of chondritic materials—including enstatite, ordinary, Rumuruti-type, and carbonaceous chondrites (Goodrich et al. 2015 and references therein). The chondritic materials are

78 equivalent to the xenolithic clasts in typical polymict ureilites.
79
80 Carbonaceous chondritic lithologies AhS 671 and AhS 91/91A were first found among the AhS
81 stones and characterized by Goodrich et al. (2019). These lithologies are xenoliths—not genetically
82 related to ureilites—consisting mainly of C1 material, enclosing minor fragments of ureilitic olivine
83 and pyroxene, as well as ordinary chondrite and enstatite chondrite fragments (Goodrich et al. 2019).
84 The C1 lithologies contain phyllosilicates (serpentine and saponite), amorphous material, magnetite,
85 breunnerite, dolomite, fayalitic olivine, an unidentified Ca-rich silicate phase, Fe, Ni sulfides, and
86 minor Ca-phosphate, and ilmenite (Goodrich et al. 2019). The bulk oxygen isotope compositions of
87 the C1 lithology are $\delta^{18}O = 13.53‰$ and $\delta^{17}O = 8.93‰$ which are unlike those of any known
88 chondrites, but similar to the compositions of several CC-like clasts in typical polymict ureilites
89 (Goodrich et al. 2019).
90
91 To elucidate the nature of the OM and the origin of carbonaceous chondritic lithologies, we
92 conducted structural, elemental and isotopic analyses of OM in AhS 671 and AhS 91A with micro-
93 Fourier transform infrared spectroscopy (μFTIR), Raman microspectroscopy, scanning transmission
94 X-ray microscopy (STXM), and elemental analyzer/isotope ratio mass spectrometry (EA/IRMS). We
95 further characterized AhS 671 with nanoscale secondary isotope mass spectrometry (NanoSIMS) and
96 secondary electron microscopy (SEM).
97
98 **METHODS**
99 **Bulk Carbon and Nitrogen Contents and Their Isotopic Compositions**
100 For the measurements of total carbon and nitrogen contents and their isotopic compositions, we used
101 an automated EA/IRMS system (Flash EA1112 elemental analyzer/Conflo III interface/Delta Plus
102 XP isotope-ratio mass spectrometer, Thermo Finnigan Co., Bremen) at JAMSTEC, which was
103 modified to improve the sensitivity for small sample analysis (>100 ngN, >500 ngC) (Isaji et al. 2020;

Ogawa et al. 2010). This analysis was conducted at the same time by the same methods as our previous measurement of the carbonaceous clast in the Zag meteorite (Kebukawa et al. 2020). Subsamples of AhS 671 and AhS 91A were rinsed with an organic solvent mixture (dioxin-analysis-grade dichloromethane and methanol, FUJIFILM Wako Pure Chemical Corporation, Japan, 1:1 by volume) to remove contaminants from the surface, and then dried under a gentle flow of argon gas at ambient temperature. Sample aliquots weighing 12 to 629 μg were weighed in a pre-cleaned tin capsule (3.5 × 4 mm smooth wall capsules, Ludi Co., Swiss) and folded into a small packet before being introduced into the EA/IRMS. The forceps and tin capsules used in this study were pre-cleaned in the mixed solvent described above. The carbon and nitrogen contents and their isotopic compositions were calibrated using three reference materials covering from −34.17‰ to +0.49‰ for $\delta^{13}C$ and from +0.86‰ to +61.53‰ for $\delta^{15}N$, including: L-tyrosine (BG-T; C: 59.7%, N: 7.74%, $\delta^{13}C$: −20.83±0.10‰, $\delta^{15}N$: +8.74±0.09‰) (Tayasu et al. 2011), nickel octaethylporphyrin (Ni-OEP; C: 73.0%, N: 9.47%, $\delta^{13}C$: −34.17±0.06‰, $\delta^{15}N$: +0.86±0.03‰) (Ogawa et al. 2010), L-valine (USGS75; C: 51.3 %, N: 12.0%, $\delta^{13}C$: +0.49±0.07‰, $\delta^{15}N$: +61.53±0.14‰) (Schimmelmann et al. 2016). The analytical errors for the isotopic compositions estimated by repeated analyses of BG-T and Ni-OEP are ±0.39‰ (s.d. 1σ, n=11, 0.58–12.8 μgC) for $\delta^{13}C$ and ±0.66‰ (s.d. 1σ, n=12, 0.08–1.7 μgN) for $\delta^{15}N$.

Micro Fourier Transform Infrared Spectroscopy

For micro-FTIR analysis, a small amount of material from the clasts was pressed between two KBr plates (~5 × 5 × 1 mm^3). IR absorption spectra were collected using a micro-FTIR (JASCO FT/IR-6100+IRT-5200), equipped with a ceramic IR light source, a germanium-coated KBr beam splitter, a mercury-cadmium-telluride (MCT) detector, and ×16 Cassegrain mirrors, at Yokohama National University. A total of 256 scans of IR transmission spectra were accumulated with a wavenumber resolution of 4 cm^{-1}, in the wavenumber range of 7000-400 cm^{-1}, with a 50 × 50 μm^2 aperture.

Background spectra were acquired through blank areas of the KBr adjacent to the samples.

Raman Microspectroscopy

A few hundred micrometer-sized grains from AhS 671 and AhS 91A were pressed into gold substrates (0.1 mm-thick) with glass slides, and analyzed using a Raman microspectrometer (Nanophoton RAMANtouch) with a 532 nm laser at JAMSTEC. The spot size was <1 μm using ×100 objective with the numerical aperture of 0.90, and the laser power at the sample surface was <700 μW. The spectral range was 100–2600 cm^{-1} with a 600 grooves/mm grating. The exposure time for each spectrum was 20 s and two accumulations were obtained for each analytical spot to discard cosmic ray events in the detector. The Raman shift was calibrated using a silicon wafer prior to analyses.

The peak positions (ω_D and ω_G), the full width at half-maximum (FWHM, Γ_D and Γ_G), and the peak intensity ratio (I_D/I_G) of defect (D: ~1350 cm^{-1}) band and graphite (G: ~1590 cm^{-1}) band were determined by peak fitting to the Lorentzian and BWF (Breit–Wigner–Fano), respectively—so called L–BWF model (Ferrari and Robertson 2000)—with a linear baseline correction between 900-1800 cm^{-1}, following the method in Kiryu et al. (2020).

FIB

Ultrathin sections (approximately 100 nm thick) were prepared from AhS 671 and AhS 91A using a focused ion beam (FIB) apparatus (SMI-4050), at Kochi Institute for Core Sample Research, JAMSTEC. The sections (14 × 12 × 0.1 μm^3 for AhS 671 and 12 × 10 × 0.1 μm^3 for AhS 91A) were extracted using the FIB with a Ga^+ ion beam at 30 kV then finished with a lower accelerating voltage of 5 kV. These sections were mounted on a commercial FIB grid with W deposition.

STXM/XANES

Carbon X-ray absorption near-edge structure (C-XANES) analyses were performed using the STXM at beamline 5.3.2.2 of the Advanced Light Source (ALS), Lawrence Berkeley National Laboratory (Kilcoyne et al. 2003). Microspectral images stacks at the C *K*-edge were acquired with energy step sizes (ΔE) of 0.1 eV in 283-295.5 eV region, 0.5 eV in 280-283 eV and 295.5-301.0 eV regions, and 1 eV in 301-310 eV region, with a dwell time of 5 ms and 0.1-0.2 μm steps per pixel. C-XANES peak intensity maps were obtained from these image data sets. An image representing the amount of aromatic/olefinic C was obtained by subtracting the optical density (OD, –ln(transmission/I_0)) image at 283 eV (pre-edge) from that at 285.2 eV. Similarly, a carbonate image was defined as the difference between the OD at 290.2 eV and that at 289.5 eV. Energy calibration was performed using the C 1s → $3s\sigma_g$ transition of CO_2 gas at 292.74 eV (Prince et al. 1999).

Fe-XANES analyses were performed using the STXM at BL4U of the UVSOR, Institute for Molecular Science. The Fe L_3-edge-XANES spectra were acquired with ΔE of 0.2 eV in 705-724 eV region, and 1 eV in 700-705 eV and 724-730 eV regions, with a dwell time of 3 ms and 0.2 μm steps per pixel. The Fe-XANES spectral component map was obtained using the singular value decomposition (SVD) method (e.g., Koprinarov et al. 2002) from a "stack" image data set, in order to visualize the distribution of three different spectral components. Energy calibration was performed using the F 1s → a_{1g} transition of SF_6 gas at 688 eV.

The elemental maps were obtained by acquiring pairs of images below (I_1) and on the absorption edges (I_2), at 280 and 292 eV, respectively for C *K*-edge, 525 eV and 539 eV for O *K*-edge, and 705 eV and 709 eV for Fe L_3-edge, with a dwell time of 3-5 ms, and taking the $-\ln(I_2/I_1)$ for each pixel, with 0.05-0.1 μm steps per pixel. STXM/XANES data analysis was performed using the software aXis2000 (http://unicorn.mcmaster.ca/aXis2000.html).

NanoSIMS

After the STXM, we analyzed the FIB-prepared-sections of AhS 671 and AhS 91A by ion imaging with the JAMSTEC NanoSIMS 50L at Kochi Institute for Core Sample Research, JAMSTEC. A typical measurement involved rastering a focused primary Cs^+ beam (~100 nm diameter, ~1 pA) across 18 × 18 μm^2 areas for AhS 671 and 24 × 24 μm^2 areas for AhS 91A (256 × 256 pixels) for 20 cycles with an acquisition time of 5 ms/pixel (328 sec/frame). The ^{12}C, ^{13}C, ^{16}O, $^{12}C^{14}N$, $^{12}C^{15}N$, and ^{32}S were measured as negative secondary ions simultaneously in six electron multipliers. Secondary electrons were detected along with the secondary ions.

After C and N isotope analysis of the sample, we conducted a measurement of H isotopes (^1H and ^2H) and ^{12}C as negative secondary ions together with secondary electrons. A focused Cs^+ primary beam (~200 nm diameter, ~3 pA) was rastered over 18 × 18 μm^2 areas for AhS 671 and 24 × 24 μm^2 areas for AhS 91A, and 256 × 256 pixel images were acquired for 20 cycles with an acquisition time of 10 ms/pixel (655 sec/frame).

Measurement was started after stabilization of the secondary ion intensities following a pre-sputtering procedure of approximately 10 min. The sample was coated with a 10 nm Au thin film to mitigate electrostatic charging on the surface. The final images were generated from regions that had statistically enough counts. The carbon-rich regions were chosen by distributions of ^{12}C within a section applying 10% threshold of total ^{12}C ion counts. The H, C and N isotopic compositions were calculated following analytical routines using a standard organic material (1-hydroxybenzotriazole hydrate; $C_6H_5N_3O{\cdot}xH_2O$) (Ito et al. 2014). The isotopic images were processed using the custom written software "NASA JSC imaging software for NanoSIMS" developed in the Interactive Data Language (IDL) program (Ito and Messenger 2008).

Secondary Electron Microscopy

Back-scattered electron images (BEI), elemental X-ray maps, and transmission Kikuchi diffraction

(TKD) measurements were obtained from the FIB slice of AhS 671 using a Supra 55 variable pressure FEG-SEM with a Bruker Electron Back-Scattered Diffraction (EBSD) system in the Materials Evaluation Laboratory, Structural Engineering Division, Johnson Space Center (JSC). X-ray mapping on the Supra 55 FEG-SEM utilized a Bruker energy dispersive spectrometer (EDS). We previously determined that a column pressure of 9 Pa and no C-coating on the sample was optimal for TKD. We used 320 × 240 pattern pixelation, frame averaging of 3, 20 kV, a working distance of 14.9 mm, pixel size of 1.95 μm, and low extractor voltage to yield an acceptable balance of hit rate, mapping speed and map quality using an exposure time of 30 ms (gain 650). The TKD maps took 1 to 9 h to acquire.

RESULTS

Bulk Elemental and Isotopic Analyses

The bulk C and N abundances and the $\delta^{13}C$ and $\delta^{15}N$ values of AhS 671 and AhS 91A are summarized in Table 1 and Fig. 1. These values were considerably different between AhS 671 and 91A. The C abundances in AhS 91A were smaller than in AhS 671. The N abundances in AhS 91A were much smaller than in AhS 671, and thus N/C ratios of AhS 91A were smaller than in AhS 671. The C and N abundances and isotope ratios were variable among each AhS 91A sample aliquots, indicating high heterogeneity in this sample compared with AhS 671 (at least among our AhS 91A and AhS 671 sample aliquots).

Table 1. Bulk C and N elemental and isotope analysis of AhS 671 and AhS 91A.

		Sample weight (mg)	C wt%	$\delta^{13}C$ ‰	N wt%	$\delta^{15}N$ ‰	N/C at.
AhS 671	Run#1	0.052	3.6	-4.3	0.17	+52.5	0.040
	Run#2	0.093	4.0	-4.3	0.20	+47.6	0.043
	Run#3	0.043	4.0	-3.0	0.21	+51.4	0.044
	Average		**3.9 ±0.2**	**-3.8 ±0.7**	**0.19 ±0.02**	**+50.5 ±2.6**	**0.042 ±0.002**

AhS 91A	Run#1	0.012	4.8		-29.0		0.056		n.d.	0.010	
	Run#2	0.033	2.1		-13.9		0.045		n.d.	0.018	
	Run#3	0.092	0.8		-14.1		0.012		n.d.	0.011	
	Run#4	0.214	n.d.		n.d.		n.d.		n.d.	n.d.	
	Run#5	0.177	1.3		-11.2		0.033		+133	0.023	
	Run#6	0.629	0.2		-3.9		0.007		n.d.	0.025	
	Run#7	0.435	0.1		-9.5		0.009		n.d.	0.058	
				±1.		**±9.**		**±0.02**			**±0.01**
	Average		**1.6**	**7**	**-13.6**	**1**	**0.027**	**1**		**0.024**	**8**

Errors are standard deviation (1σ). n.d.= not determined.

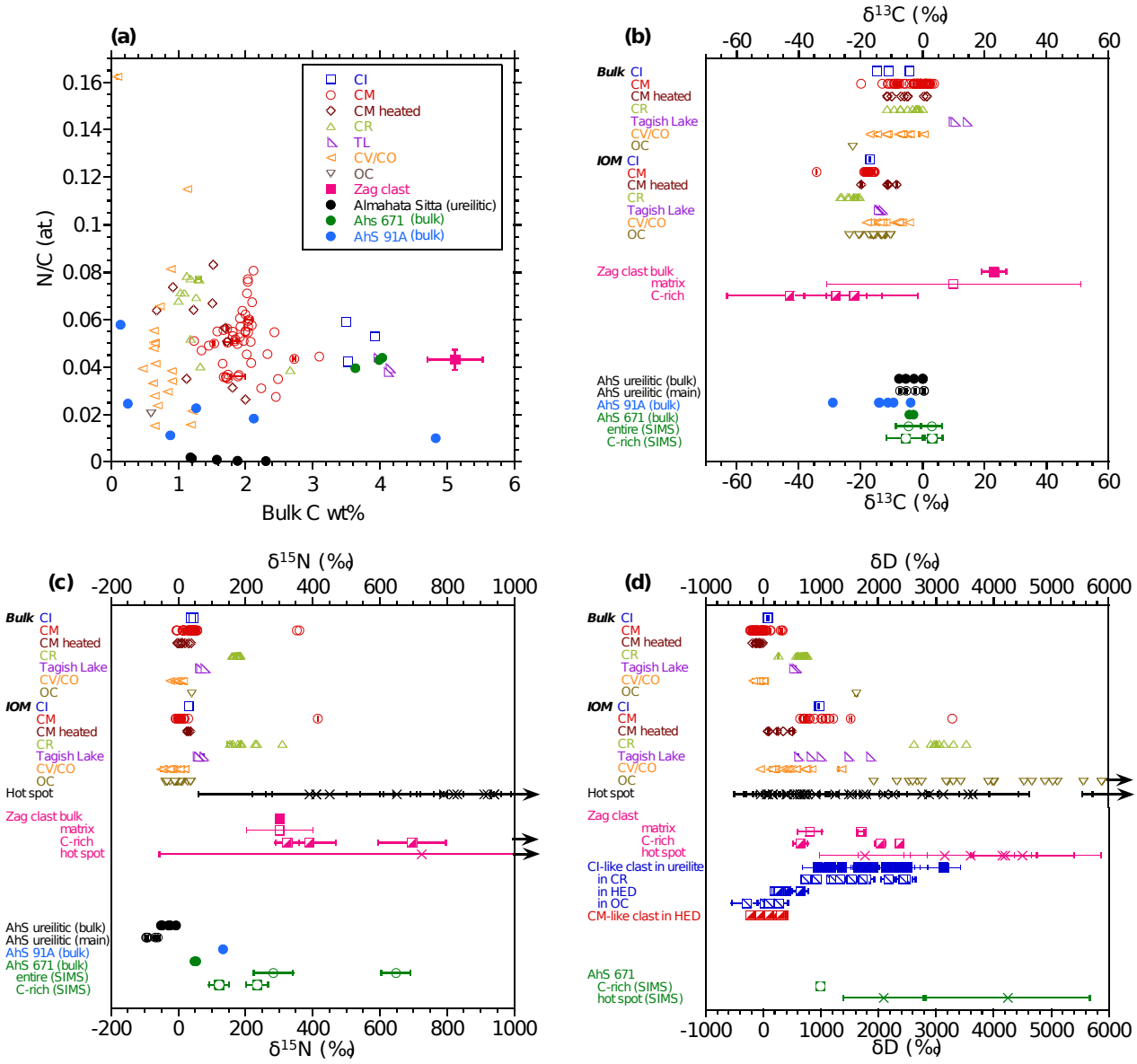

230

231 Fig. 1: Elemental and isotopic composition of AhS samples 91A and 671 compared with previously
232 obtained values for various chondrites, AhS ureilitic lithologies, CI- and CM-like clasts in ureilites,
233 and a xenolithic clast in the Zag ordinary chondrite. (a) Bulk C abundance (wt.%) vs. N/C ratio
234 (atomic), (b) $\delta^{13}C$, (c) $\delta^{15}N$, and (d) δD. Data from Alexander et al. (2007, 2010) for IOM from
235 chondrites; Herd et al. (2011) for Tagish Lake IOM; Alexander et al. (2012) for bulk chondrites;
236 Busemann et al. (2006) and Hashiguchi et al. (2015) for hot spots; Downes et al. (2015) for AhS
237 ureilitic lithologies; Kebukawa et al. (2019b, 2020) for the Zag clast; Patzek et al. 2020 GCA for CI-

238 and CM-like clasts.

239

240 **Micro-FTIR Spectra**

241 Fig. 2 shows IR absorption spectra of AhS 671 and AhS 91A. Little to no organic features were
242 visible in both AhS 671 and AhS 91A at around 2900 cm^{-1} where aliphatic C–H peaks appear.
243 Enlarged and baseline corrected spectra in the region of aliphatic C-H (Fig. 2, lower panel) showed
244 small peaks at 2960, 2920-30, and 2855 cm^{-1} due to aliphatic CH_3 asymmetric stretching, aliphatic
245 CH_2 asymmetric stretching, and aliphatic CH_3+CH_2 symmetric stretching, respectively. Considering
246 that control spectra (baked antigorite) showed no peaks at this region, these peaks in AhS 671 and
247 AhS 91A are likely indigenous. The CH_2/CH_3 peak height ratios were ~2.4 for both AhS 671 and
248 AhS 91A, which was much higher than the values of typical CCs (~1-1.5: (Kebukawa et al. 2019a).

249

250 The IR spectrum of AhS 671 showed a broad band around 3400 cm^{-1} with a shoulder at 3677 cm^{-1}
251 which was characteristic of phyllosilicate OH with some adsorbed/interlayer water. A peak at 1010
252 cm^{-1} was consistent with Si–O in phyllosilicates. Small shoulders at 1080, 955, and 885 cm^{-1} were
253 likely due to Ca-rich pyroxene. A peak at 1440 cm^{-1} was assigned to carbonates. A peak at 1640 cm^{-1}
254 can be assigned to adsorbed/interlayer water. The IR spectrum of AhS 91A only showed silicate
255 features with the peaks at 972 and 880 cm^{-1}, and small shoulders at 1065, 940, and 835 cm^{-1}. These
256 silicate features were likely due to olivine with some contribution of pyroxene, considering that
257 olivine is known to have main Si–O peaks at ~990-960 cm^{-1} and ~890-870 cm^{-1} with a small peak at
258 ~950-930 cm^{-1}, in which higher Mg numbers tend to have these peaks at higher wavenumber
259 (Salisbury et al. 1991). Also, diopside has Si–O peaks at ~1080 cm^{-1}, 970 cm^{-1}, and 870 cm^{-1} with a
260 small peak at ~920 cm^{-1}, and enstatite shows Si–O peaks at ~1080-1060 cm^{-1} and ~1010 cm^{-1} with a
261 small peaks at ~960-930 cm^{-1} (Salisbury et al. 1991).

262

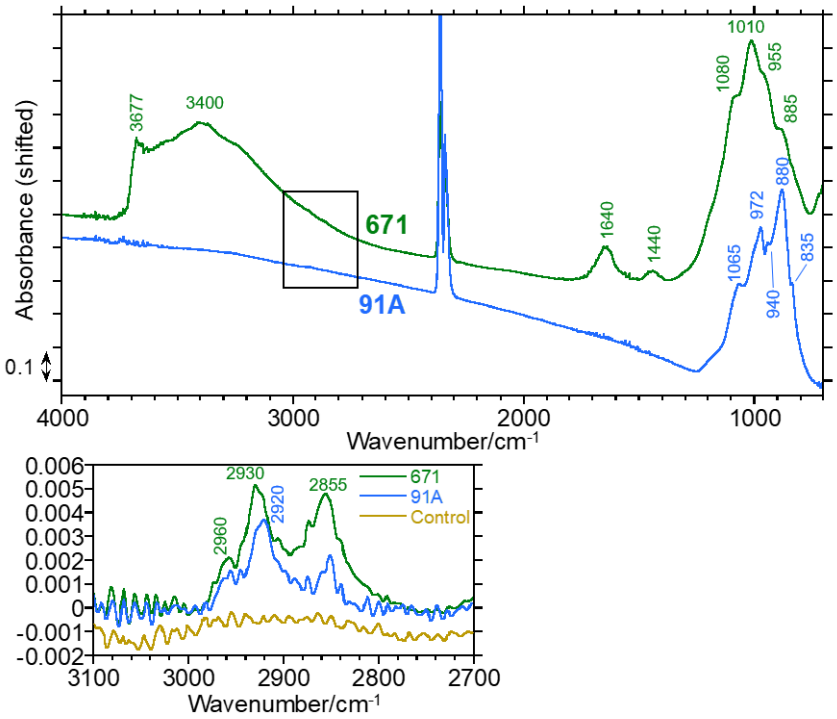

Fig. 2: Infrared absorption spectra of AhS 671 and AhS 91A. Enlarged aliphatic C-H regions (a linear baseline between 3100-2700 cm^{-1} was subtracted) are shown in the lower panel with control (antigorite baked at 500 °C).

Raman Spectra

Fig. 3 shows the Raman spectra of AhS 671 and AhS 91A. The D band and the G band were shown in the first order region of the Raman spectra. The peak position (ω), the FWHM (Γ), and the peak intensity ratio (I_D/I_G) of the D band and G band obtained by peak fitting are shown in Fig. 4 and Table 2. The Raman parameters of these two AhS fragments do not follow the metamorphic trends of CCs. Although AhS 91A was somewhat in between the type 2 CC group (Murchison (CM2), Tagish Lake (C2-ung), Y-793321 (CM2-heated); Kiryu et al. 2020) and the thermally metamorphosed CC group (Allende (CV3.2), Moss (CO3.6); Kiryu et al. 2020), AhS 671 was completely off from the trends and large heterogeneity was observed. The absolute intensity of D and G bands of AhS 91A were significantly lower than those of AhS 671 (Fig. 3). Although the absolute intensities are affected not only by concentration of sample but also by the surface conditions and so on, this is consistent

279 with the results of the bulk elemental analysis that AhS 91A was poor in OM (Table 1 and Fig. 1).

280

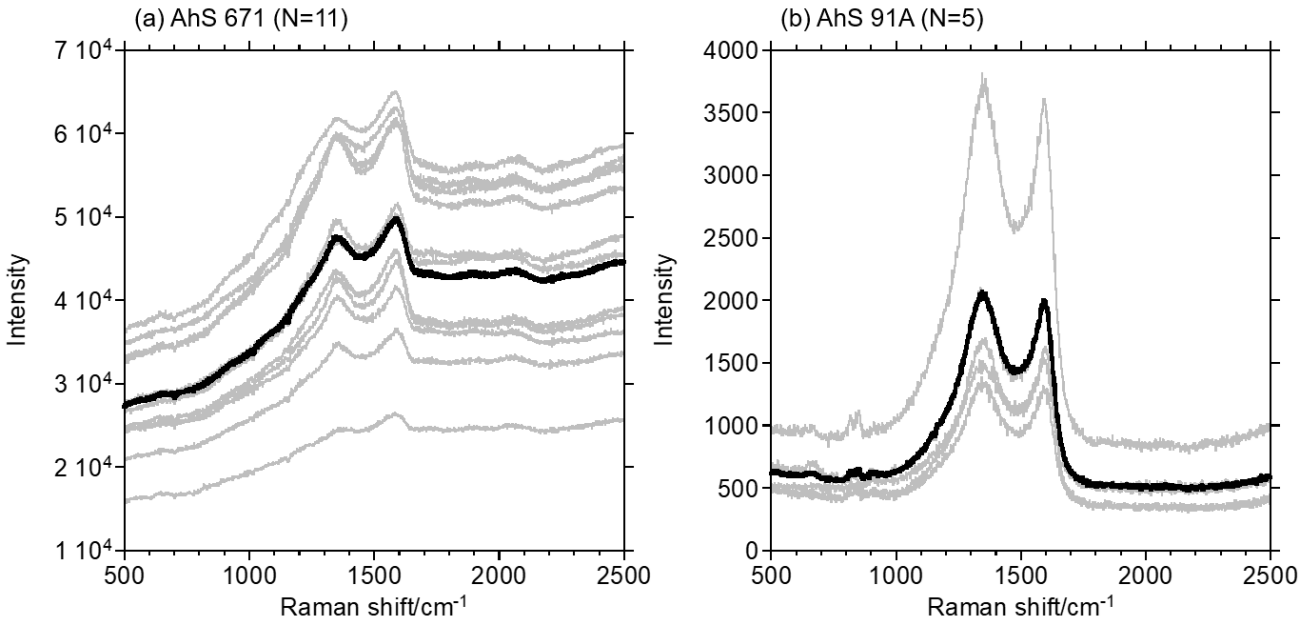

281

283 Fig. 3: Raman spectra of (a) AhS 671 and (b) AhS 91A. The spectra from each spot are shown in

284 gray, and average spectra are shown in black.

285

286

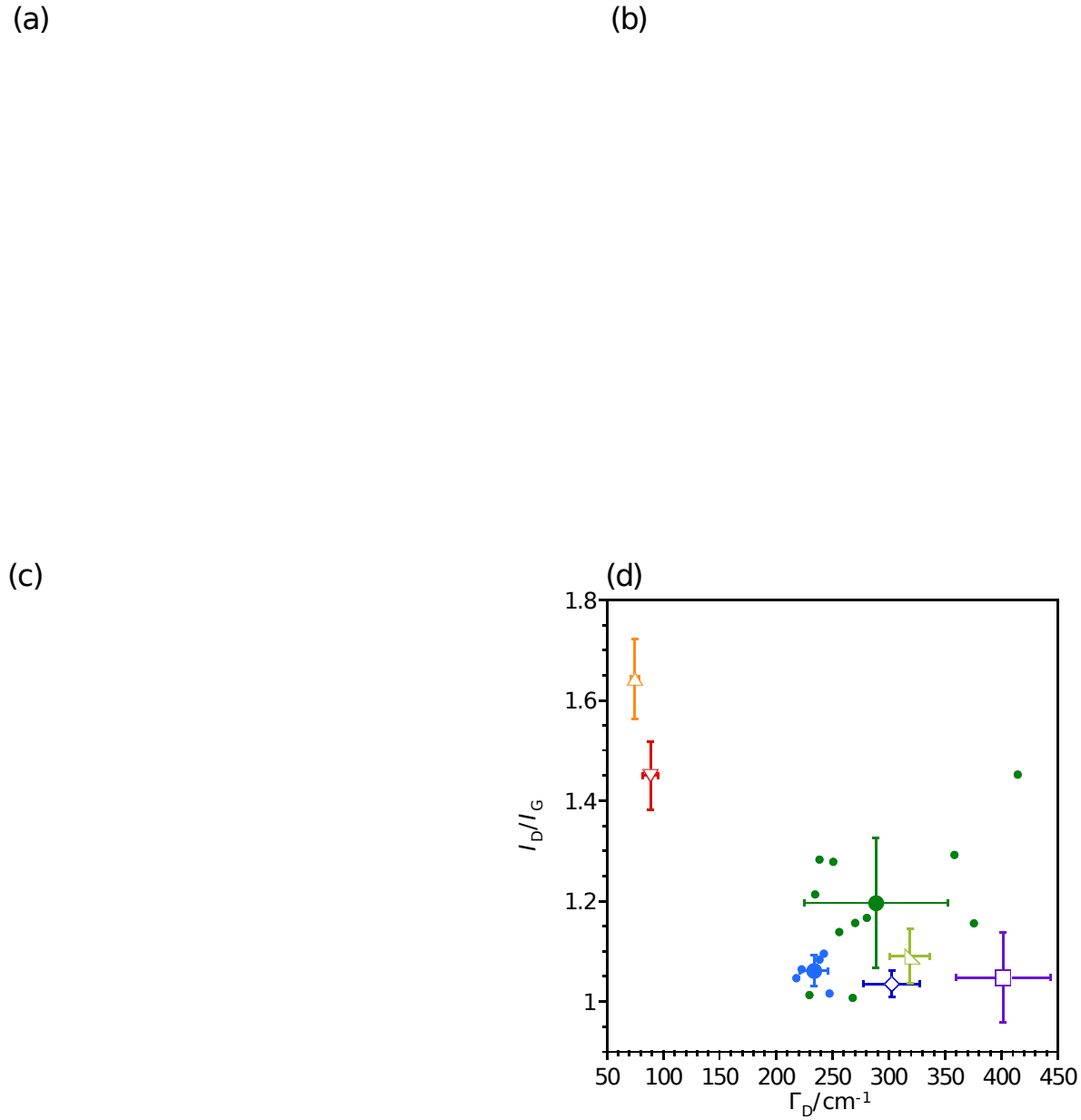

287

288 Fig. 4: The Raman D and G band parameters of AhS 671 and AhS 91A compared with various
289 carbonaceous chondrites. (a) the D band peak position vs. the full width half-maximum (FWHM) of
290 D band, (b) the G band peak position vs. FWHM of G band, (c) FWHM of G band vs. FWHM of D
291 band, and (d) FWHM of D band vs. the peak intensity ratio of D and G bands (I_D/I_G). The data of
292 Murchison (CM2), Tagish Lake (C2-ung), Allende (CV3.2), Moss (CO3.6), and Yamato (Y-)793321
293 (CM2-heated) is from Kiryu et al. (2020).

294

295 Table 2: Raman D and G band parameters of AhS 671 and AhS 91A. Chondrite data are from Kiryu

et al. (2020).

		ω_D/cm^{-1}	Γ_D/cm^{-1}	ω_G/cm^{-1}	Γ_G/cm^{-1}	I_D/I_G
AhS 671	Point#1	1343	358	1579	136.3	1.29
	Point#2	1334	268	1579	119.5	1.01
	Point#3	1339	251	1579	135.5	1.28
	Point#4	1344	234	1585	108.0	1.21
	Point#5	1343	270	1582	115.2	1.16
	Point#6	1331	414	1577	124.5	1.45
	Point#8	1336	256	1578	122.6	1.14
	Point#9	1348	375	1577	119.3	1.16
	Point#10	1340	238	1583	112.2	1.28
	Point#11	1343	280	1579	113.8	1.17
	Point#12	1343	230	1583	109.6	1.01
	Average (n=11)	1340 ± 5	289 ± 64	1580 ± 3	119.7 ± 9.5	1.20 ± 0.13
AhS 91A	Point#1	1342	218	1590	108.9	1.05
	Point#2	1346	242	1591	108.6	1.10
	Point#3	1346	247	1590	109.4	1.02
	Point#4	1347	222	1594	105.4	1.06
	Point#5	1346	238	1591	110.4	1.08
	Average (n=5)	1345 ± 2	234 ± 13	1591 ± 2	108.5 ± 1.9	1.06 ± 0.03
Tagish Lake	C2-ung	1356 ± 3	401 ± 42	1582 ± 4	97.6 ± 6.6	1.05 ± 0.09
Murchison	CM2	1351 ± 4	303 ± 25	1585 ± 2	101.1 ± 5.0	1.04 ± 0.03
Y-793321	CM2 heated	1355 ± 4	319 ± 18	1584 ± 2	101.6 ± 6.5	1.09 ± 0.05
Allende	CV3	1341 ± 3	75 ± 4	1590 ± 3	67.2 ± 3.3	1.64 ± 0.08
Moss	CO3.6	1337 ± 4	89 ± 7	1592 ± 6	73.5 ± 3.8	1.45 ± 0.07

STXM/XANES

STXM images of the FIB section taken from AhS 671 are shown in Fig. 5a and b. C-XANES spectra

from regions of interest (ROIs) in the FIB section are shown in Fig. 5c. The STXM elemental maps showed that sub-micrometer C-rich grains/aggregates were scattered over the FIB section particularly in Fe-rich regions (Fig. 5a). C-XANES spectra of the C-rich areas showed peaks at 285.0 eV assigned to aromatic/olefinic C with small features at 287.5 eV assigned to aliphatic C and at 288.7 eV assigned to carboxyl/ester C(=O)O (Fig. 5c). ROI#1 in Fig. 5b was condensed OM. The "condensed" nature was characterized by the C-XANES with low baseline (280-283 eV region) and high absorption at ~292 eV (Fig. 5c). On the other hand, ROI#2 and ROI#4 are diffused OM as seen by C-map (Fig. 5b) as well as C-XANES with higher baseline and lower absorption at ~292 eV due to lower concentration of carbon (Fig. 5c). Note that the FIB section of AhS 91A did not contain detectable amount of carbon, likely due to the large heterogeneity in micrometer scale of AhS 91A. Therefore, we focused on AhS 671 for further nanoscale analysis.

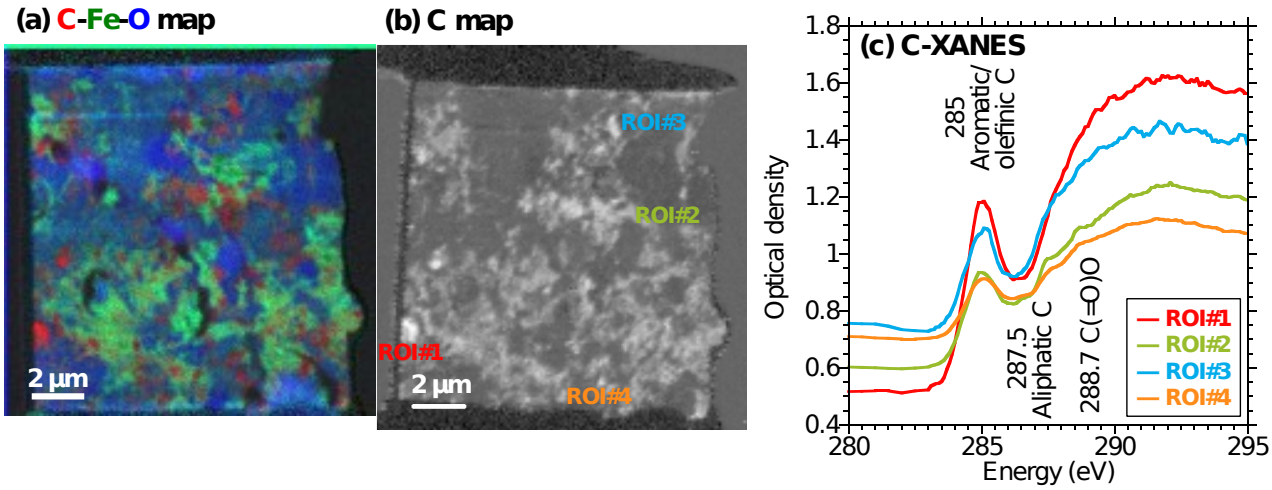

Fig. 5: (a) STXM elemental map of the FIB section from AhS 671. (b) STXM C-map with ROIs. (c) C-XANES spectra from ROIs shown in (b).

To compare the molecular structures of each area, we obtained the peak intensities at 285.0 eV (aromatic/olefinic C), 287.5 eV (aliphatic C), and 288.7 eV [C(=O)O] by subtracting a linear baseline and normalizing to the intensities at 291.5 eV (approximately at ionization potential energy) (Fig. 6).

It should be noted that functional group abundances in Fig. 6 are not exact fractions in OM, but rather the ratios are relative indicators to compare molecular structure heterogeneity among the regions. These diagrams showed that ROI#1 (condensed OM) was highly aromatic in nature, and ROIs #2 and #4 (diffused OM) were less aromatic in nature. This tendency is consistent with OM in type 1 and 2 chondrites (Le Guillou et al. 2014), but overall AhS 671 is richer in aromatics than type 1 and 2 chondrites. ROI#3 plotted off from the trends and was rich in C(=O)O and aliphatic C.

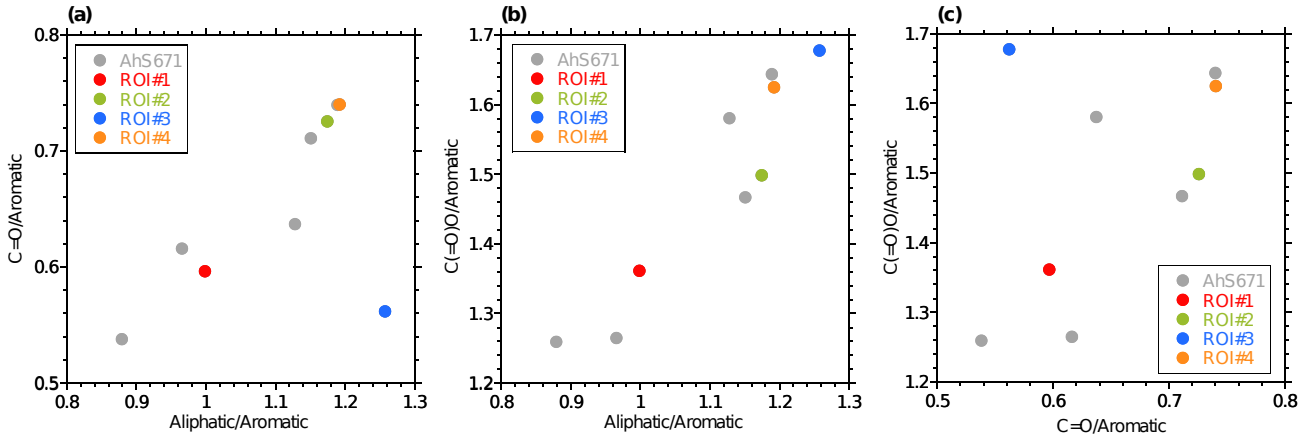

Fig. 6: C-XANES peak intensity ratios of AhS 671. The data from ROIs in Fig. 5 is indicated by color, and gray circle represents data from other regions in the FIB section.

The OM grains were distributed in the Fe-rich matrix (Fig. 5a). The Fe-XANES spectra in these regions (ROI#2 and ROI#4 in Fig. 5b) were consistent with phyllosilicates (see next section) (Fig. 7c). Fe^{2+} rich regions were clearly distinguished in the AhS 671 FIB section (green in Fig. 7a) and were likely olivine (Fig. 8), but no/little OM were found in these regions.

Using the method of Le Guillou et al. (2015) which is modified from Bourdelle et al. (2013), the Fe^{3+}/ΣFe values in silicates could be calculated by the peak intensity ratios of $R_{L3} = I_{Fe3+}/I_{total}$ using the integrated peak intensities of the Fe L_3 edge at 707.6-710.8 eV as I_{Fe3+} and 704-711 eV as I_{total};

$$\frac{Fe^{3+¿}}{\sum Fe} = \frac{R_{L_3} - 0.2614}{0.006} \%¿ \quad \text{(eq. 1)}$$

The average $Fe^{3+}/\Sigma Fe$ ratio at ROI#2 and ROI#4 was 74.9±2.7 %. This value is slightly higher than the values of silicates in CR2 chondrites (66-75%) and CM chondrites (50-70%) (Le Guillou et al. 2015 and references therein). While, employing the method of van Aken and Liebscher (2002) which could be more universal, the $Fe^{3+}/\Sigma Fe$ values were calculated with;

$$\frac{I_{L3}}{I_{L2}} = \frac{1}{a\,x^2 + bx + x} - 1 \quad \text{(eq. 2)}$$

where I_{L3} is the integrated intensity of Fe^{3+} L_3 edge (707.6-709.6 eV), I_{L2} is the integrated intensity of Fe^{2+} L_2 edge (719.0-721.0 eV), a = 0.193, b = –0.465, c = 0.366, and x = $Fe^{3+}/\Sigma Fe$. With this method, the average $Fe^{3+}/\Sigma Fe$ ratio at ROI#2 and ROI#4 was 60.3±4.2 %. This ratio is lower than the previous one, but likely closer to the actual $Fe^{3+}/\Sigma Fe$ ratio in the sample. A calibration is required to obtain the precise ratios, but it is beyond the scope of our study.

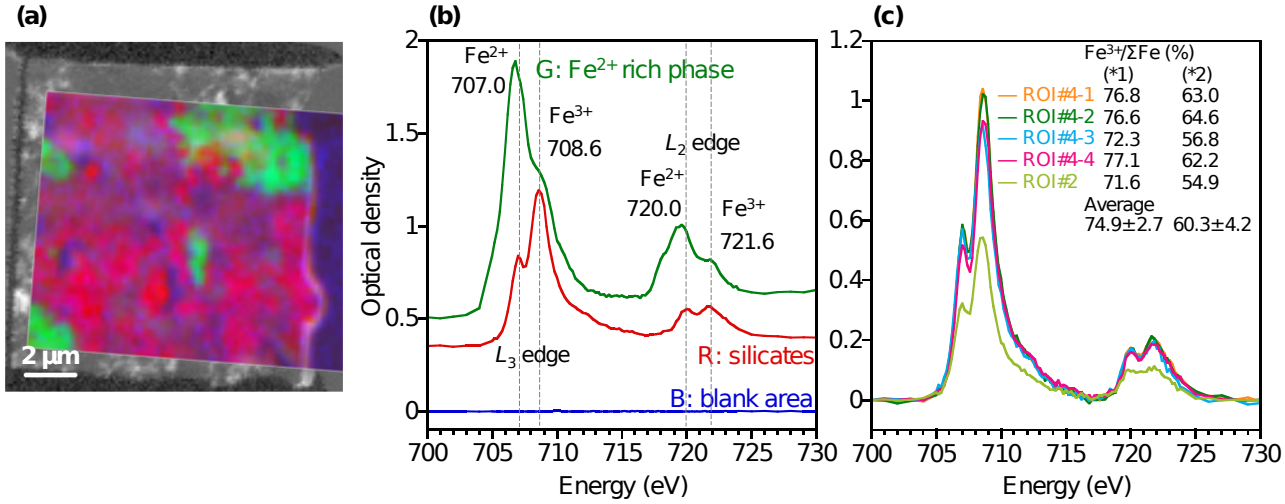

Fig. 7: (a) Fe-XANES composition map of AhS 671 based on the spectra in (b). Red: silicates, Green: Fe^{2+} rich phase, and Blue: blank area (I_0). (c) Fe-XANES spectra at ROI#2 and ROI#4 (Fig. 5b), with their $Fe^{3+}/\Sigma Fe$ (%) calculated using the methods of (*1) Le Guillou et al. (2015) and (*2) van Aken & Liebscher (2002).

Mineralogy

Fig. 8 shows the results of transmission Kikuchi diffraction (TKD) of the FIB slice of AhS 671 featured in this current paper. We identified the following crystalline phases: olivine, pyrrhotite and magnetite. Based on EDS compositions, and comparison with TEM imaging of AhS 91A (Goodrich et al. 2019) the bulk of this FIB slice consists of poorly-crystalline serpentine and saponite. One area of the FIB slice produced multiple TKD patterns for diopside. These were all individual, unconnected pixels, which must be viewed with caution. However, these were the only diopside diffraction matches in the FIB slice, and this area produced only matches to this phase. Therefore, the phases might actually be diopside. Comparison with Fig. 5 indicates that the O-rich areas in that figure contain well-crystalline olivine and possibly diopside, while the Fe-rich areas are poorly crystalline, representing the poorly-crystalline phyllosilicates observed in Goodrich et al. (2019).

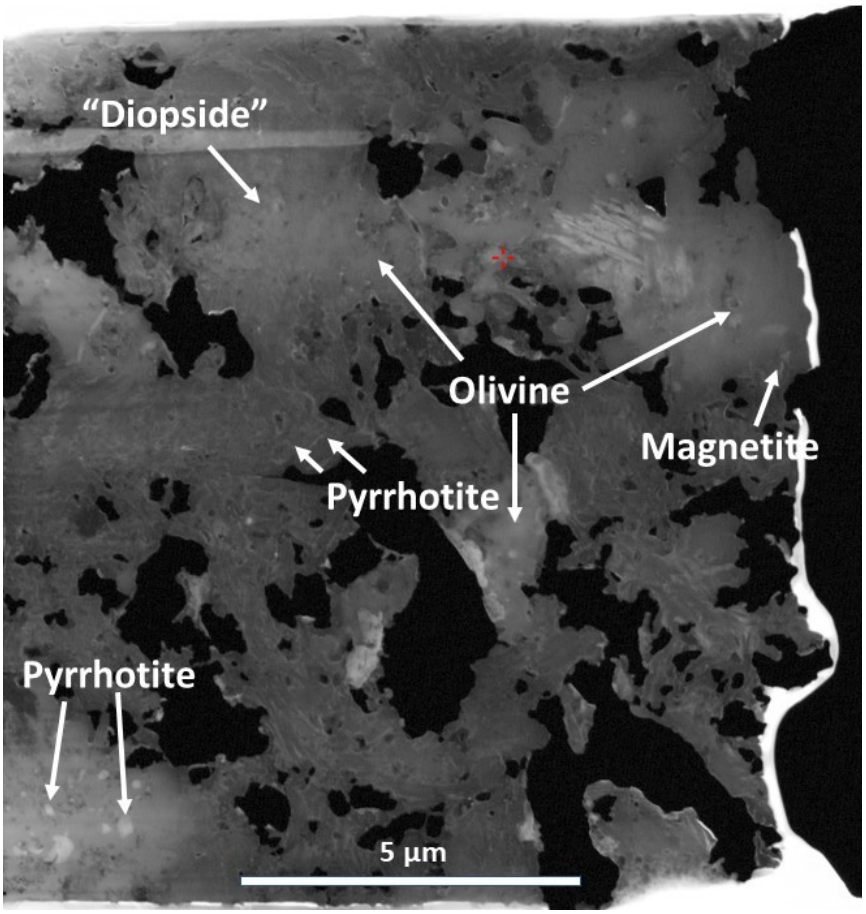

Fig. 8: Crystalline phases identified in the FIB slice if AhS 671 by TKD, shown on a BSE image. Phase identified as “Diopside” is a tentative identification.

NanoSIMS

δD, $\delta^{15}N$, and $\delta^{13}C$ values of AhS 671 obtained by NanoSIMS are shown in Table 3 and Fig. 1b-d, and elemental and isotope images are shown in Fig. 9. The average δD value of the C-rich area was approximately +1000‰, with some isotopic “hot spots” up to approximately +4000‰. The average $\delta^{15}N$ and $\delta^{13}C$ values of the C-rich area were approximately +100 to +200‰ and −5 to +3‰, respectively. An $\delta^{13}C$ anomalous area was observed with $\delta^{13}C$ values of −132±26 ‰. The C-XANES characteristics of these hot spots and the $\delta^{13}C$ anomalous area did not show significant differences from surrounding OM.

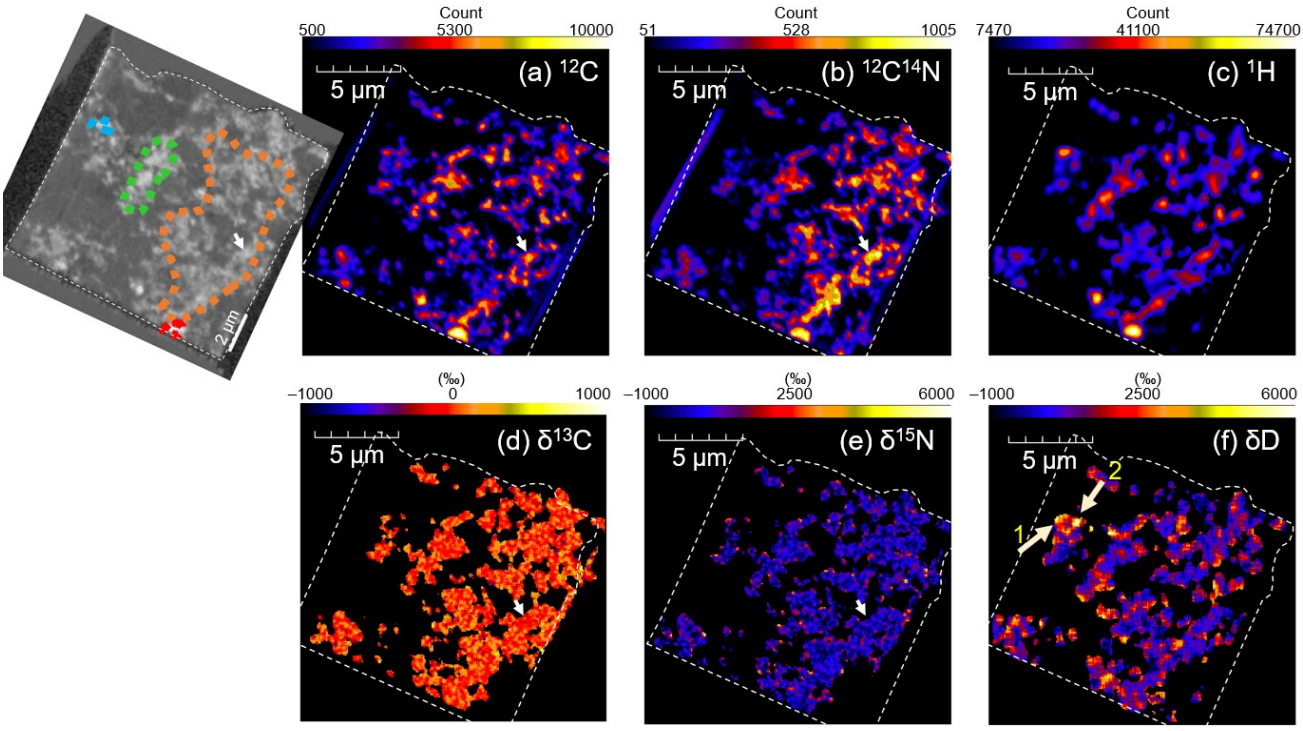

Fig. 9: NanoSIMS elemental and isotopic composition images of AhS 671. (a) ^{12}C, (b) $^{12}C^{14}N$, (c) ^{1}H, (d) $\delta^{13}C$, (e) $\delta^{15}N$, and (f) δD. Arrows in (a, b, d, e) indicate a $\delta^{13}C$ anomalous spot. Arrows in (f) indicate δD hot spots.

Table 3. $\delta^{13}C$, $\delta^{15}N$, and δD values obtained from the FIB section of AhS 671 by NanoSIMS.

AhS 671		$\delta^{13}C$ ‰		$\delta^{15}N$ ‰		δD ‰	
Run#1	Entire	−4.5	±4.1	+283	±59		
	C-rich area	−5.4	±6.2	+121	±30		
Run#2	Entire	+2.9	±3.4	+648	±44		
	C-rich area	+3.1	±3.3	+234	±32		
	C anomalous area	−132	±26	−361	±239		
Run#3	C-rich area					+988	±59
	Hot spot #1					+2087	±695
	Hot spot #2					+4246	±1430

Errors are standard deviation (1σ).

Entire: entire area analyzed, C-rich area: carbon-rich regions chosen by distributions of ^{12}C within a section applying 10% threshold of total ^{12}C ion counts, and C anomalous area: a $\delta^{13}C$ anomalous spot shown in Fig. 9.

DISCUSSION

Elemental and Isotopic Characteristics

Elemental and isotopic characteristics of OM reflect degrees of alteration and metamorphism, and thus these characteristics can be used to evaluate its origin as well as for classification of its host meteorite (Alexander et al. 2007; Alexander et al. 2010). In summary, the elemental and isotopic compositions of AhS 671 are similar to those of diverse CCs, but do not exactly match with any known groups. High abundances of bulk C with moderate N/C ratios in AhS 671 compared to various chondrites, were close to the values of CI chondrites and Tagish Lake (Alexander et al. 2012) (Fig. 1a). However, the bulk $\delta^{13}C$ of AhS 671 was rather close to CM and CR chondrites, while $\delta^{15}N$ is consistent with CI, CM, and Tagish Lake (Alexander et al. 2012) (Fig. 1c). The NanoSIMS analysis allows us to obtain microscale $\delta^{13}C$, $\delta^{15}N$, and δD values on C-rich areas (most likely organics) in AhS 671. The $\delta^{13}C$ values of the C-rich areas and the entire areas were consistent with the bulk AhS

671 value. However, the $\delta^{15}N$ values of the C-rich areas were higher than the bulk value and close to CR chondrites (Alexander et al. 2012), and the entire areas were even higher than the C-rich areas (up to ~650‰) (Fig. 1b, c). The differences in the $\delta^{15}N$ among bulk and NanoSIMS entire and C-rich areas could be due to local heterogeneities of N-compounds and/or the presence of inorganic N-bearing compounds. The δD values of C-rich areas in AhS 671 were similar to the IOM from CI, CM, and Tagish Lake (Alexander et al. 2007; Alexander et al. 2010; Herd et al. 2011), but much higher if compared to the values of bulk chondrites (Alexander et al. 2012) (Fig. 1d).

The elemental and isotopic compositions of AhS 91A fragments showed large heterogeneity. In general, C and N abundances were lower than in AhS 671 (Table 1 and Fig. 1a). The $\delta^{13}C$ of AhS 91A was slightly lower than AhS 671, the $\delta^{15}N$ could be higher than AhS 671, although we could obtain the $\delta^{15}N$ values from only a single fragment of AhS 91A due to the small sample size (<100 ng of N) (Table 1 and Fig. 1b,c). Loss of C and N could be explained by the thermal processing, but differences in $\delta^{15}N$ between AhS 671 and AhS 91A rather indicate differences in origin of OM. The elemental and isotopic compositions of both AhS 671 and AhS 91A are clearly distinguished from those ureilitic lithologies of AhS (Downes et al. 2015) (Fig. 1), consistent with the fact that AhS 671 and AhS 91A are xenoliths and the amount of ureilitic material in these lithologies is small (Goodrich et al. 2019).

Molecular Structures of Organic Matter in AhS 671 and AhS 91A

The infrared spectra of AhS 671 and AhS 91A showed that OM—at least aliphatic-containing OM—was not very abundant, and such bulk IR features were consistent with local observation by C-XANES. The small aliphatic C-H peaks and their relatively high CH_2/CH_3 peak intensity ratios were similar to IR characteristics of type 3 chondrites such as Kaba (CV3.0/3.1) (Kebukawa et al. 2011; Kebukawa et al. 2019a) and heated CM chondrites (Quirico et al. 2018).

Raman D and G band parameters are a good indicator for degree of thermal processing of macromolecular OM. The Raman parameters of both AhS 671 and AhS 91A were somewhat unique among chondrites (Fig. 4). The D band parameters (Γ_D and ω_D) of AhS 671 indicate slight heating, while the G band parameters plotted in the opposite direction to the heating trend (Fig. 4a,b). The D band parameters of AhS 91A were also indicative of slight heating. The Γ_G and I_D/I_G values of AhS 91A were close to type 2 chondrites (Tagish Lake, Murchison, and Y-793321), but the ω_G was close to thermally metamorphosed type 3 CCs (Allende and Moss) (Fig. 4b,d). Such mixed Raman features are likely due to highly aromatic but not graphene-like structures. It is consistent with the C-XANES spectra which show high aromatic content but not the 1s-σ* exciton peak at 291.7 eV due to graphene structures (Cody et al. 2008). These trends were somewhat similar to the experimentally-heated Tagish Lake and Murchison meteorites (Chan et al. 2019; Kiryu et al. 2020). The high Γ_G values of AhS 671 and AhS 91A could be explained by an increase in development in the sizes of crystalline domains without graphitic ordering (Chan et al. 2019). These Raman characteristics are indicative of short-term heating—possibly by impact.

Some of the ureilitic stones from AhS contain disordered carbonaceous compounds as well as crystalline graphite and diamond (Jenniskens et al. 2009; Kaliwoda et al. 2013). Kaliwoda et al. (2013) showed zones which consist of different carbon phases and large areas with disordered graphitic material, accompanied with some tiny patches of crystalline graphite as revealed by Raman mapping analysis. Although no genetic relationship is suspected between the carbonaceous materials in ureilitic lithologies and those in AhS 671 and AhS 91A, the Raman spectrum of the most "disordered" phase in Kaliwoda et al. (2013) is similar to our AhS 671 spectra.

Local heterogeneity of OM in the micron to submicrometer scale is observed in AhS 671 by STXM/C-XANES. In general, globule-like or compacted OM shows more aromatic nature, and diffused OM

455 is less aromatic and contains more O-bearing functional groups. These trends are consistent with
456 type 1 and 2 chondrites, and soluble OM may contribute to diffuse OM (Le Guillou et al. 2014). The
457 C-XANES spectra of AhS 671 are characterized by fewer aliphatic and O-bearing functional groups
458 compared to type 1 and 2 chondrites (Le Guillou et al. 2014), and these characteristics are consistent
459 with mild heating perhaps by impact processing.
460
461 The OM-rich area (e.g., ROI#4 in Fig. 5) was also rich in Fe^{3+} (Fig. 7) and this region likely consisted
462 poorly-crystalline phyllosilicates. The associations of OM with phyllosilicates or amorphous silicates
463 were well known for CCs in submicrometer scale (Abreu and Brearley 2010; Changela et al. 2018; Le
464 Guillou et al. 2014; Le Guillou and Brearley 2014; Vinogradoff et al. 2017; Vollmer et al. 2014). The
465 $Fe^{3+}/\Sigma Fe$ ratios in this region were slightly higher than the values of silicates in type 2 chondrites (Le
466 Guillou et al. 2015 and references therein). Since decreases in Fe^{3+} indicate progressive alteration due
467 to the transfer of Fe^{3+} from silicates to oxides (Le Guillou et al. 2015), the OM rich areas in AhS 671
468 may not have been subjected to progressive aqueous alteration.
469
470 **Comparison between AhS 671 and carbonaceous chondritic clasts in various meteorites**
471 Overall, our analyses of AhS 671 are consistent with a C1 lithology but distinguished from known
472 groups of CCs, as discussed by Goodrich et al. (2019). Goodrich et al. (2019) discussed comparisons
473 between this lithology and other known xenolithic CC-like clasts in brecciated meteorites. Thus, we
474 extend that comparison using our data for AhS 671.
475
476 Visser et al. (2018) estimated peak metamorphic temperatures of 30 volatile-rich clasts (16 CI-, and
477 14 CM-like clasts) in 10 different host meteorites (4 polymict ureilites, 5 polymict eucrites, and 1
478 howardite) by Raman carbon thermometry. They showed that the peak temperatures experienced by
479 CI-like clasts and CM-like clasts ranged between 30–110 °C with an average of 65 ± 25 °C, and
480 between 50–110 °C with an average of 70 ± 25 °C, respectively, indicating that they had not

experienced peak temperatures higher than typical CM and CI chondrites. On the other hand, our Raman investigations of AhS 671 indicated slight heating somewhat similar to insoluble organic matter (IOM) from Y-86720, a heated CM chondrite with the heating stage of IV (>750 °C) (Nakamura 2005), whose Raman parameters were ω_D = 1348.6±0.3 cm^{-1}, Γ_D = 244.7±0.5 cm^{-1}, ω_G = 1583.4±0.3 cm^{-1}, Γ_D = 96.0±0.2 cm^{-1}, and I_D/I_G = 1.16±0.05 (Busemann et al. 2007). Note that our Raman D and G band parameters are comparable to those in Busemann et al. (2007) but not to those in Visser et al. (2018) due to the difference in the fitting methods employed (Kiryu et al. 2020).

Patzek et al. (2020) reported that δD values of CI-like clasts in polymict ureilites (DaG 319, DaG 999, and EET 83309) range from +950 to +3100‰, and those in CR chondrites (Al Rais and Renazzo) have δD values from +740 to +2480‰ (Fig. 1d), while CI-like clasts in NWA 7542 (an HED meteorite) have δD values from +200 to +640‰, and δD in a CI-like clast in the ordinary chondrite Sahara 98645 ranges from −290 to +270‰. δD values of five CM-like clasts in the HED meteorites (NWA 7542, Sariçiçek, and EET 87513) range from −220 to +340‰ (Patzek et al. 2020). The δD of AhS 671 is ~1000‰ and in the range of CI-like clasts in polymict ureilites and in CR chondrites (Fig. 1d). The OM in clasts in DaG 999 have a primitive nature as shown by Raman parameters with estimated peak metamorphic temperatures of less than 100 °C (Visser et al. 2018), and thus at least the clasts in DaG 999 are distinguished from AhS 671.

The Zag meteorite (an H3-6 ordinary chondrite) hosts a unique CC-like clast likely originating from a primitive body such as D/P asteroids (Kebukawa et al. 2019b; Kebukawa et al. 2020; Zolensky et al. 2017), as well as xenolithic halite particles, some included within the CC clast (Chan et al. 2018; Rubin et al. 2002). Compared to the CC-like clast in the Zag meteorite, C, N, H-isotopic characteristics of AhS 671 are not very close (Fig. 1). The C-XANES features of AhS 671 (Fig. 5c) are somewhat similar to the C-rich aggregate in the Zag clast (Kebukawa et al. 2019b), but not similar

506 to other OM phases in the Zag clast (Kebukawa et al. 2020). C-rich aggregates were found in a type 3
507 ordinary chondrite, Sharps (Brearley 1990), but their C-XANES characteristics are rather graphitic
508 (Kebukawa et al. 2017), and thus well distinguished from AhS 671. On the other hand, a carbon rich
509 clast in a CR2 chondrite, LaPaz Icefield 02342, is rich in O-bearing functional groups in C-XANES
510 with the average values of $\delta D \approx +130‰$ and $\delta^{15}N \approx 0‰$ (Nittler et al. 2019), and these
511 characteristics are distinguished from AhS 671.
512
513 Overall, AhS 671 shows some similarities to, but does not exactly match any known CC-like clasts,
514 although there are not enough data for a full comparison. As suggested by Patzek et al. (2020), the C1
515 clasts in several meteorite groups prove the existence of additional primitive, volatile-rich material in
516 the early Solar System, besides the samples available as the CI, CM, and CR chondrites. The C1-
517 lithologies of AhS support the idea that there are much larger diversities in the CC parent bodies than
518 these we already sampled.
519
520 **Implications for Origin of AhS CC-lithologies**
521 As described in detail by Goodrich et al. (2019), AhS 91A and AhS 671 are dominated by a hydrous
522 CC lithology consisting of fine-grained phyllosilicates (serpentine and saponite) and amorphous
523 material, magnetite, bruennerite, dolomite, olivine (Fo 28-42), an unidentified Ca-rich silicate phase,
524 pyrrhotite, pentlandite, Ca-phosphate and ilmenite. The mineralogy we determined from the FIB of
525 AhS 671 is consistent with the previous work, except for our still tentative identification of diopside.
526 These stones have obvious mineralogic similarities to CI1 chondrites, but the Ca-rich silicate
527 (tentatively identified as consisting mainly of dehydrated saponite) and magnetite-fayalite
528 assemblages indicate heterogeneous post-aqueous alteration thermal metamorphism. The bulk oxygen
529 isotope composition of AhS 91A ($\delta^{18}O = 13.53‰$, $\delta^{17}O = 8.93‰$) is unlike that of any known CC,
530 but is essentially identical to that of a C1 clast in the Nilpena polymict ureilite (Goodrich et al. 2019).
531

Goodrich et al. (2019) suggested that AhS 671 and AhS 91A were likely derived from the same original carbonaceous chondritic parent body, but that they experienced different degrees of thermal processing, higher in AhS 671 than in AhS 91A. Our organic analyses of these lithologies are generally consistent with this idea, but suggest that the degree of thermal processing is actually higher in AhS 91A than in AhS 671 as indicated by C abundances. Such an inconsistency could be due to sample heterogeneity, as we see large heterogeneities in elemental and isotopic analysis in AhS 91A (Fig. 1a). Our analyses of OM molecular structures showed evidence of slight heating, likely short-term heating possibly by impact, rather than long-term thermal metamorphism induced by decay of radioactive nuclides. Such impact heating could have occurred at the original parent body of AhS 671 and AhS 91A, rather than at the time of implantation into the ureilitic parent body. However, there are some differences between AhS 671 and AhS 91A which cannot be explained only by different degrees of heating. There were likely at least two reservoirs of OM as indicated by isotopic signatures (see Discussion, Elemental and Isotopic Characteristics).

CONCLUSIONS

Organic matter in the xenolithic carbonaceous chondritic lithologies of Almahata Sitta (AhS), AhS 671 and AhS 91A showed unique features indicating that they represent CC-like material not previously sampled in our meteorite collection:

1. Elemental and isotopic analyses of AhS 671 and AhS 91A indicate primitive, outer Solar System origin of their parent body, and there were likely at least two reservoirs of OM.

2. Raman D and G band parameters of AhS 671 and AhS 91A indicate slight heating, likely short-term heating possibly by impact, rather than long-term thermal metamorphism induced by decay of radioactive nuclides.

3. The small aliphatic C-H peaks of AhS 671 and AhS 91A in the IR spectra and their relatively high CH_2/CH_3 peak intensity ratios were similar to type 3 chondrites and heated CM chondrites. The C-XANES spectra of AhS 671 are characterized by fewer aliphatic and O-bearing functional groups as compared to primitive type 1 and 2 chondrites. These IR and C-XANES features are consistent with mild heating perhaps by impact induced heating process.

4. C1-lithologies of AhS support the idea that there are much larger diversities in primitive carbonaceous chondritic materials in the Solar System than those we have already sampled.

Acknowledgements

We thank the Associated Editor Scott Sandford and an anonymous reviewer for their fruitful comments. This work was supported by JSPS KAKENHI (grant numbers JP17H06458, JP18K03722, and JP19H05073). The operations of the Advanced Light Source are supported by the Director, Office of Science, Office of Basic Energy Sciences, US Department of Energy under Contract No. DE-AC02-05CH11231. MZ and JM were supported by the NASA Emerging Worlds Program.

References

Abreu N. M. and Brearley A. J. 2010. Early solar system processes recorded in the matrices of two highly pristine CR3 carbonaceous chondrites, MET 00426 and QUE 99177. *Geochimica et Cosmochimica Acta* 74:1146-1171.

Alexander C. M. O. D., Bowden R., Fogel M. L., Howard K. T., Herd C. D., and Nittler L. R. 2012. The provenances of asteroids, and their contributions to the volatile inventories of the terrestrial planets. *Science* 337:721-723.

Alexander C. M. O. D., Fogel M., Yabuta H., and Cody G. D. 2007. The origin and evolution of chondrites recorded in the elemental and isotopic compositions of their macromolecular organic matter. *Geochimica et Cosmochimica Acta* 71:4380-4403.

Alexander C. M. O. D., Newsome S. D., Fogel M. L., Nittler L. R., Busemann H., and Cody G. D. 2010. Deuterium enrichments in chondritic macromolecular material—Implications for the

origin and evolution of organics, water and asteroids. *Geochimica et Cosmochimica Acta* 74:4417-4437.

Bourdelle F., Benzerara K., Beyssac O., Cosmidis J., Neuville D. R., Brown G. E., and Paineau E. 2013. Quantification of the ferric/ferrous iron ratio in silicates by scanning transmission X-ray microscopy at the Fe $L_{2,3}$ edges. *Contributions to Mineralogy and Petrology* 166:423-434.

Brearley A. J. 1990. Carbon-rich aggregates in type 3 ordinary chondrites: Characterization, origins, and thermal history. *Geochimica et Cosmochimica Acta* 54:831-850.

Busemann H., Alexander C. M. O. D., and Nittler L. R. 2007. Characterization of insoluble organic matter in primitive meteorites by microRaman spectroscopy. *Meteoritics & Planetary Science* 42:1387-1416.

Busemann H., Young A. F., Alexander C. M. O., Hoppe P., Mukhopadhyay S., and Nittler L. R. 2006. Interstellar chemistry recorded in organic matter from primitive meteorites. *Science* 312:727-730.

Chan Q. H. S., Nakato A., Kebukawa Y., Zolensky M. E., Nakamura T., Maisano J. A., Colbert M. W., Martinez J. E., Kilcoyne A. L. D., Suga H., Takahashi Y., Takeichi Y., Mase K., and Wright I. P. 2019. Heating experiments of the Tagish Lake meteorite: Investigation of the effects of short-term heating on chondritic organics. *Meteoritics & Planetary Science* 54:104-125.

Chan Q. H. S., Zolensky M. E., Kebukawa Y., Fries M., Ito M., Steele A., Rahman Z., Nakato A., Kilcoyne A. L. D., Suga H., Takahashi Y., Takeichi Y., and Mase K. 2018. Organic matter in extraterrestrial water-bearing salt crystals. *Science advances* 4:eaao3521.

Changela H. G., Le Guillou C., Bernard S., and Brearley A. J. 2018. Hydrothermal evolution of the morphology, molecular composition, and distribution of organic matter in CR (Renazzo-type) chondrites. *Meteoritics & Planetary Science* 53:1006-1029.

Cody G. D., Alexander C. M. O. D., Yabuta H., Kilcoyne A. L. D., Araki T., Ade H., Dera R., Fogel M., Militzer B., and Mysen B. O. 2008. Organic thermometry for chondritic parent bodies. *Earth and Planetary Science Letters* 272:446-455.

Collinet M. and Grove T. L. 2020. Incremental melting in the ureilite parent body: Initial composition, melting temperatures, and melt compositions. *Meteoritics & Planetary Science* 55:832-856.

Downes H., Abernethy F. A. J., Smith C. L., Ross A. J., Verchovsky A. B., Grady M. M., Jenniskens P., and Shaddad M. H. 2015. Isotopic composition of carbon and nitrogen in ureilitic fragments of the Almahata Sitta meteorite. *Meteoritics & Planetary Science* 50:255-272.

Ferrari A. C. and Robertson J. 2000. Interpretation of Raman spectra of disordered and amorphous carbon. *Physical Review B* 61:14095-14107.

Goodrich C. A., Hartmann W. K., O'Brien D. P., Weidenschilling S. J., Wilson L., Michel P., and Jutzi M. 2015. Origin and history of ureilitic material in the solar system: The view from asteroid 2008 TC 3 and the Almahata Sitta meteorite. *Meteoritics & Planetary Science*

50:782-809.

Goodrich C. A., Van Orman J. A., and Wilson L. 2007. Fractional melting and smelting on the ureilite parent body. *Geochimica et Cosmochimica Acta* 71:2876-2895.

Goodrich C. A., Zolensky M. E., Fioretti A. M., Shaddad M. H., Downes H., Hiroi T., Kohl I., Young E. D., Kita N. T., Hamilton V. E., Riebe M. E. I., Busemann H., Macke R. J., Fries M., Ross D. K., and Jenniskens P. 2019. The first samples from Almahata Sitta showing contacts between ureilitic and chondritic lithologies: Implications for the structure and composition of asteroid 2008 TC3. *Meteoritics & Planetary Science* 54:2769-2813.

Hashiguchi M., Kobayashi S., and Yurimoto H. 2015. Deuterium- and ^{15}N-signatures of organic globules in Murchison and Northwest Africa 801 meteorites. *Geochemical Journal* 49:377-391.

Herd C. D. K., Blinova A., Simkus D. N., Huang Y., Tarozo R., Alexander C. M. O. D., Gyngard F., Nittler L. R., Cody G. D., Fogel M. L., Kebukawa Y., Kilcoyne A. L. D., Hilts R. W., Slater G. F., Glavin D. P., Dworkin J. P., Callahan M. P., Elsila J. E., De Gregorio B. T., and Stroud R. M. 2011. Origin and evolution of prebiotic organic matter as inferred from the Tagish Lake meteorite. *Science* 332:1304-1307.

Isaji Y., Ogawa N. O., Boreham C. J., Kashiyama Y., and Ohkouchi N. 2020. Evaluation of δ13C and δ15N Uncertainties Associated with the Compound-Specific Isotope Analysis of Geoporphyrins. *Analytical Chemistry* 92:3152-3160.

Ito M. and Messenger S. 2008. Isotopic imaging of refractory inclusions in meteorites with the NanoSIMS 50L. *Applied Surface Science* 255:1446-1450.

Ito M., Uesugi M., Naraoka H., Yabuta H., Kitajima F., Mita H., Takano Y., Karouji Y., Yada T., Ishibashi Y., Okada T., and Abe M. 2014. H, C, and N isotopic compositions of Hayabusa category 3 organic samples. *Earth, Planets and Space* 66:91.

Jenniskens P., Shaddad M. H., Numan D., Elsir S., Kudoda A. M., Zolensky M. E., Le L., Robinson G. A., Friedrich J. M., Rumble D., Steele A., Chesley S. R., Fitzsimmons A., Duddy S., Hsieh H. H., Ramsay G., Brown P. G., Edwards W. N., Tagliaferri E., Boslough M. B., Spalding R. E., Dantowitz R., Kozubal M., Pravec P., Borovicka J., Charvat Z., Vaubaillon J., Kuiper J., Albers J., Bishop J. L., Mancinelli R. L., Sandford S. A., Milam S. N., Nuevo M., and Worden S. P. 2009. The impact and recovery of asteroid 2008 TC3. *Nature* 458:485-488.

Kaliwoda M., Hochleitner R., Hoffmann V. H., Mikouchi T., Gigler A. M., and Schmahl W. W. 2013. New Raman Spectroscopic Data of the Almahata Sitta Meteorite. *Spectroscopy Letters* 46:141-146.

Kebukawa Y., Alexander C. M. O. D., and Cody G. D. 2011. Compositional diversity in insoluble organic matter in type 1, 2 and 3 chondrites as detected by infrared spectroscopy. *Geochimica et Cosmochimica Acta* 75:3530–3541.

Kebukawa Y., Alexander C. M. O. D., and Cody G. D. 2019a. Comparison of FT-IR spectra of bulk and acid insoluble organic matter in chondritic meteorites: An implication for missing carbon

663 during demineralization. *Meteoritics & Planetary Science* 54:1632–1641.
664 Kebukawa Y., Ito M., Zolensky M. E., Greenwood R. C., Rahman Z., Suga H., Nakato A., Chan Q.
665 H., Fries M., and Takeichi Y. 2019b. A novel organic-rich meteoritic clast from the outer solar
666 system. *Scientific reports* 9:3169.
667 Kebukawa Y., Nakashima S., and Zolensky M. E. 2010. Kinetics of organic matter degradation in the
668 Murchison meteorite for the evaluation of parent-body temperature history. *Meteoritics &*
669 *Planetary Science* 45:99-113.
670 Kebukawa Y., Zolensky M. E., Chan Q. H. S., Nagao K., Kilcoyne A. L. D., Bodnar R. J., Farley C.,
671 Rahman Z., Le L., and Cody G. D. 2017. Characterization of carbonaceous matter in
672 xenolithic clasts from the Sharps (H3.4) meteorite: Constraints on the origin and thermal
673 processing. *Geochimica et Cosmochimica Acta* 196:74-101.
674 Kebukawa Y., Zolensky M. E., Ito M., Ogawa N. O., Takano Y., Ohkouchi N., Nakato A., Suga H.,
675 Takeichi Y., Takahashi Y., and Kobayashi K. 2020. Primordial organic matter in the xenolithic
676 clast in the Zag H chondrite: Possible relation to D/P asteroids. *Geochimica et Cosmochimica*
677 *Acta* 271:61-77.
678 Kilcoyne A., Tyliszczak T., Steele W., Fakra S., Hitchcock P., Franck K., Anderson E., Harteneck B.,
679 Rightor E., and Mitchell G. 2003. Interferometer-controlled scanning transmission X-ray
680 microscopes at the Advanced Light Source. *Journal of synchrotron radiation* 10:125-136.
681 Kiryu K., Kebukawa Y., Igisu M., Shibuya T., Zolensky M. E., and Kobayashi K. 2020. Kinetics in
682 thermal evolution of Raman spectra of chondritic organic matter to evaluate thermal history
683 of their parent bodies. *Meteoritics & Planetary Science* in press.
684 Koprinarov I. N., Hitchcock A. P., McCrory C. T., and Childs R. F. 2002. Quantitative Mapping of
685 Structured Polymeric Systems Using Singular Value Decomposition Analysis of Soft X-ray
686 Images. *The Journal of Physical Chemistry B* 106:5358-5364.
687 Le Guillou C., Bernard S., Brearley A. J., and Remusat L. 2014. Evolution of organic matter in
688 Orgueil, Murchison and Renazzo during parent body aqueous alteration: In situ investigations.
689 *Geochimica et Cosmochimica Acta* 131:368-392.
690 Le Guillou C. and Brearley A. 2014. Relationships between organics, water and early stages of
691 aqueous alteration in the pristine CR3.0 chondrite MET 00426. *Geochimica et Cosmochimica*
692 *Acta* 131:344-367.
693 Le Guillou C., Changela H. G., and Brearley A. J. 2015. Widespread oxidized and hydrated
694 amorphous silicates in CR chondrites matrices: Implications for alteration conditions and H_2
695 degassing of asteroids. *Earth and Planetary Science Letters* 420:162-173.
696 Mittlefehldt D. W., McCoy T. J., Goodrich C. A., and Kracher A. 1998. Non-chondritic meteorites
697 from asteroidal bodies. In *Planetary materials* (ed. J. J. Papike), pp. 4-1–4-195. Mineralogical
698 Society of America, Washington, D.C.
699 Nakamura T. 2005. Post-hydration thermal metamorphism of carbonaceous chondrites. *Journal of*
700 *Mineralogical and Petrological Sciences* 100:260-272.

Nittler L. R., Stroud R. M., Trigo-Rodríguez J. M., De Gregorio B. T., Alexander C. M. O. D., Davidson J., Moyano-Cambero C. E., and Tanbakouei S. 2019. A cometary building block in a primitive asteroidal meteorite. *Nature Astronomy* 3:659-666.

Ogawa N. O., Nagata T., Kitazato H., and Ohkouchi N. 2010. Ultra sensitive elemental analyzer/isotope ratio mass spectrometer for stable nitrogen and carbon isotope analyses. In *Earth, life, and isotopes* (eds. N. Ohkouchi, I. Tayasu, and K. Koba), pp. 339-353. Kyoto University Press.

Orthous-Daunay F.-R., Piani L., Flandinet L., Thissen R., Wolters C., Vuitton V., Poch O., Moynier F., Sugawara I., and Naraoka H. 2019. Ultraviolet-photon fingerprints on chondritic large organic molecules. *Geochemical Journal* 53:21-32.

Patzek M., Hoppe P., Bischoff A., Visser R., and John T. 2020. Hydrogen isotopic composition of CI- and CM-like clasts from meteorite breccias – Sampling unknown sources of carbonaceous chondrite materials. *Geochimica et Cosmochimica Acta* 272:177-197.

Prince K. C., Avaldi L., Coreno M., Camilloni R., and Simone M. d. 1999. Vibrational structure of core to Rydberg state excitations of carbon dioxide and dinitrogen oxide. *Journal of Physics B: Atomic, Molecular and Optical Physics* 32:2551-2567.

Quirico E., Bonal L., Beck P., Alexander C. M. O. D., Yabuta H., Nakamura T., Nakato A., Flandinet L., Montagnac G., Schmitt-Kopplin P., and Herd C. D. K. 2018. Prevalence and nature of heating processes in CM and C2-ungrouped chondrites as revealed by insoluble organic matter. *Geochimica et Cosmochimica Acta* 241:17-37.

Rubin A. E., Zolensky M. E., and Bodnar R. J. 2002. The halite-bearing Zag and Monahans (1998) meteorite breccias: Shock metamorphism, thermal metamorphism and aqueous alteration on the H-chondrite parent body. *Meteoritics & Planetary Science* 37:125-141.

Salisbury J. W., Walter L. S., Vergo N., and D'Aria D. M. 1991. *Infrared (2.1–25 micrometers) spectra of minerals*. John Hopkins University Press, Baltimore.

Schimmelmann A., Qi H., Coplen T. B., Brand W. A., Fong J., Meier-Augenstein W., Kemp H. F., Toman B., Ackermann A., and Assonov S. 2016. Organic reference materials for hydrogen, carbon, and nitrogen stable isotope-ratio measurements: caffeines, *n*-alkanes, fatty acid methyl esters, glycines, L-valines, polyethylenes, and oils. *Analytical Chemistry* 88:4294-4302.

Schmitt-Kopplin P., Gabelica Z., Gougeon R. D., Fekete A., Kanawati B., Harir M., Gebefuegi I., Eckel G., and Hertkorn N. 2010. High molecular diversity of extraterrestrial organic matter in Murchison meteorite revealed 40 years after its fall. *Proceedings of the National Academy of Sciences of the United States of America* 107:2763-2768.

Scott E. R. D., Taylor G. J., and Keil K. 1993. Origin of ureilite meteorites and implications for planetary accretion. *Geophysical Research Letters* 20:415-418.

Tayasu I., Hirasawa R., Ogawa N. O., Ohkouchi N., and Yamada K. 2011. New organic reference materials for carbon-and nitrogen-stable isotope ratio measurements provided by Center for Ecological Research, Kyoto University, and Institute of Biogeosciences, Japan Agency for

Marine-Earth Science and Technology. *Limnology* 12:261-266.

van Aken P. A. and Liebscher B. 2002. Quantification of ferrous/ferric ratios in minerals: new evaluation schemes of Fe L23electron energy-loss near-edge spectra. *Physics and Chemistry of Minerals* 29:188-200.

Vinogradoff V., Le Guillou C., Bernard S., Binet L., Cartigny P., Brearley A. J., and Remusat L. 2017. Paris vs. Murchison: Impact of hydrothermal alteration on organic matter in CM chondrites. *Geochimica et Cosmochimica Acta* 212:234-252.

Visser R., John T., Menneken M., Patzek M., and Bischoff A. 2018. Temperature constraints by Raman spectroscopy of organic matter in volatile-rich clasts and carbonaceous chondrites. *Geochimica et Cosmochimica Acta* 241:38-55.

Vollmer C., Kepaptsoglou D., Leitner J., Busemann H., Spring N. H., Ramasse Q. M., Hoppe P., and Nittler L. R. 2014. Fluid-induced organic synthesis in the solar nebula recorded in extraterrestrial dust from meteorites. *Proceedings of the National Academy of Sciences of the United States of America* 111:15338-15343.

Warren P. H. and Kallemeyn G. W. 1992. Explosive volcanism and the graphite oxygen fugacity buffer on the parent asteroid(s) of the ureilite meteorites. *Icarus* 100:110-126.

Zolensky M. E., Bodnar R. J., Yurimoto H., Itoh S., Fries M., Steele A., Chan Q. H.-S., Tsuchiyama A., Kebukawa Y., and Ito M. 2017. The search for and analysis of direct samples of early Solar System aqueous fluids. *Philosophical Transactions of the Royal Society A* 375:20150386.